

1 **Fluorescence lidar observations of wildfire smoke inside cirrus: A contribution to smoke-**
2 **cirrus - interaction research**

3 Igor Veselovskii¹, Qiaoyun Hu², Albert Ansmann³, Philippe Goloub², Thierry Podvin², Mikhail
4 Korenskiy¹

5 *¹Prokhorov General Physics Institute of the Russian Academy of Sciences, Moscow, Russia.*

6 *²Univ. Lille, CNRS, UMR 8518 - LOA - Laboratoire d'Optique Atmosphérique, Lille, 59000,*
7 *France*

8 *³Leibniz Institute for Tropospheric Research, Leipzig, Germany*

9 **Correspondence:** Igor Veselovskii (iveselov@hotmail.com)

10 **Abstract**

11 A remote sensing method, based on fluorescence lidar measurements, that allows to detect and to
12 quantify the smoke content in upper troposphere and lower stratosphere (UTLS) is presented.
13 The unique point of this approach is that, smoke and cirrus properties are observed in the same
14 air volume simultaneously. In this article, we provide results of fluorescence and
15 multiwavelength Mie-Raman lidar measurements performed at ATOLL observatory from
16 Laboratoire d'Optique Atmosphérique, University of Lille, during strong smoke episodes in the
17 summer and autumn seasons of 2020. The aerosol fluorescence was induced by 355 nm laser
18 radiation and the fluorescence backscattering was measured in a single spectral channel, centered
19 at 466 nm and having 44 nm width. To estimate smoke particle properties, such as number,
20 surface area and volume concentration, the conversion factors, which link the fluorescence
21 backscattering and the smoke microphysical properties, are derived from the synergy of
22 multiwavelength Mie-Raman and fluorescence lidar observations. Based on two case studies, we
23 demonstrate that the fluorescence lidar technique provides the possibility to estimate the smoke
24 surface area concentration within freshly formed cirrus layers. This value was used in smoke INP
25 parameterization scheme to predict ice crystal number concentrations in cirrus generation cells.

26
27 **Introduction**

28 Aerosol particles in the upper tropospheric and lower stratospheric (UTLS) height regime
29 play an important role in processes of heterogeneous ice formation, however our current
30 understanding of these processes is still insufficient for a trustworthy implementation in

numerical weather and climate prediction models. The ability of aerosol particles to act as ice nucleating particles (INP) depends on meteorological factors such as temperature and ice supersaturation (as a function of vertical velocity), as well as on the aerosol type in the layer in which cirrus developed (Kanji et al., 2017). Heterogeneous ice nucleation initiated by insoluble inorganic materials such as mineral dust has been studied since a long time (e.g., DeMott et al. 2010, 2015; Hoose and Möhler, 2012; Murray et al., 2012; Boose et al., 2016; Schrod et al., 2017; Ansmann et al. 2019b), while the potential of omnipresent organic particles, especially of frequently occurring aged, long-range-transported wildfire smoke particles, to act as INP is less well explored and thus not well understood (Knopf et al., 2018). Wildfire smoke can reach the lower stratosphere via pyro-cumulonimbus (pyroCb) convection (Fromm et al., 2010; Peterson et al., 2018, 2021; Hu et al., 2019; Khaykin et al., 2020) or via self-lifting processes (Boers et al., 2010, Ohneiser et al., 2021). It is widely assumed that the ability of smoke particles to serve as INP mainly depends on the organic material (OM) in the shell of the coated smoke particles (Knopf et al., 2018), but may also depend on mineral components in the smoke particles (Jahl et al., 2021). The ice nucleation efficiency may increase with increasing duration of the long-range transport as Jahl et al. (2021) suggested. Disregarding the progress made in this atmospheric research field during the last years, the link between ice nucleation efficiency and the smoke particle chemical and morphological properties is still largely unresolved (China et al., 2017; Knopf et al., 2018).

To contribute to the field of smoke-cirrus-interaction research, we present a laser remote sensing method that allows us simultaneously to detect and quantify the smoke particles amount inside of cirrus layers together with cirrus properties and to provide INP estimates in regions close to the cloud top where ice formation usually begins. The unique point of our approach is that, for the first time, smoke and cirrus properties are observed in the same air volume simultaneously. Recently, a first attempt (closure study) was performed to investigate the smoke impact on High Arctic cirrus formation (Engelmann et al. 2021). However, the aerosol measurements had to be performed outside the clouds layers, and then an assumption was needed that the estimated aerosol (and estimated INP) concentration levels also hold inside the cirrus layers. Now, we propose a method to directly determine INP-relevant smoke parameters inside the cirrus layer during ice nucleation events. This also offers the opportunity to illuminate whether an INP reservoir can be depleted in cirrus evolution processes or not. Furthermore, this

63 new lidar detection method permits a clear discrimination between, e.g., smoke and mineral dust
64 INPs.

65 Multiwavelength Mie-Raman lidars or High Spectral Resolution lidars (HSRL) are
66 favorable instruments to provide the vertical profiles of the physical properties of tropospheric
67 aerosol particles. In particular, the inversion of the so-called $3\beta+2\alpha$ lidar observations, based on
68 the measurement of height profiles of three aerosol backscatter coefficients at 355, 532, and 1064
69 nm and two extinction coefficients at 355 and 532 nm, allows us to estimate smoke
70 microphysical properties (Müller et al., 1999, 2005; Veselovskii et al., 2002, 2015). However,
71 the aerosol content in UTLS height range can be low, so that particle extinction coefficients
72 cannot be determined with sufficient accuracy and are thus not available in the lidar inversion
73 data analysis. To resolve this issue Ansmann et al. (2019a, 2021) used the synergy of
74 polarization lidar measurements and Aerosol Robotic Network (AERONET) sunphotometer
75 observations (Holben et al., 1998) to derive conversion factors (to convert backscatter
76 coefficients into microphysical particle properties) and to estimate INP concentrations for dust
77 and smoke aerosols with the retrieved aerosol surface area concentration as aerosol input.

78 Dust particles are very efficient ice nuclei in contrast to wildfire smoke particles. In this
79 context, the question arises: How can we unambiguously discriminate smoke from dust
80 particles? This is realized by integrating a fluorescence channel into a multiwavelength aerosol
81 lidar (Reichardt et al., 2017; Richardson et al., 2019; Veselovskii et al., 2020; 2021). The
82 fluorescence capacity of smoke (ratio of fluorescence backscattering to the overall aerosol
83 backscattering), significantly exceeds corresponding values for other types of aerosol, such as
84 dust or anthropogenic particles (Veselovskii et al., 2020; 2021), and thus allows us to
85 discriminate smoke from other aerosol types. The fluorescence technique provides therefore the
86 unique opportunity to monitor ice formation in well identified wildfire smoke layers, and thus to
87 create a good basis for long-term investigations of smoke cirrus interaction.

88 In this article, we present results of fluorescence and multiwavelength Mie-Raman lidar
89 measurements performed at the ATOLL (ATmospheric Observation at liLLe) of the Laboratoire
90 d'Optique Atmosphérique, University of Lille, during strong smoke episodes in the summer and
91 autumn seasons of 2020. The results demonstrate that the fluorescence lidar is capable to monitor
92 the smoke in the UTLS height range and inside the cirrus clouds formed at or below the
93 tropopause. We start with a brief description of the experimental setup in Sect.2. In the first part

94 of the result section (Sect.3.1 and 3.2), it is explained how smoke optical properties can be
95 quantified by using fluorescence backscattering information and how we can estimate smoke
96 microphysical properties (volume, surface area, and number concentration) from measured
97 fluorescence backscatter coefficients. In this approach, multiwavelength Mie-Raman aerosol
98 lidar observations are used in addition. The retrieved values of the smoke particle surface area
99 concentration are then the aerosol input in the smoke INP estimation. A case study is discussed
100 in Sect.3.2. Two case studies are then presented in Sect.3.3 to demonstrate the capability of a
101 fluorescence lidar to monitor ice formation in extended smoke layers and to provide detailed
102 information on aerosol microphysical properties and smoke-relate INP concentration levels.

103

104 **2. Experimental setup**

105 The multiwavelength Mie-Raman lidar LILAS (LIlle Lidar AtmosphereS) is based on a
106 tripled Nd:YAG laser with a 20 Hz repetition rate and pulse energy of 70 mJ at 355 nm.
107 Backscattered light is collected by a 40 cm aperture Newtonian telescope and the lidar signals
108 are digitized with Licel transient recorders of 7.5 m range resolution, allowing simultaneous
109 detection in the analog and photon counting mode. The system is designed for simultaneous
110 detection of elastic and Raman backscattering, allowing the so called $3\beta+2\alpha+3\delta$ data
111 configuration, including three particle backscattering ($\beta_{355}, \beta_{532}, \beta_{1064}$), two extinction ($\alpha_{355}, \alpha_{532}$)
112 coefficients along with three particle depolarization ratios ($\delta_{355}, \delta_{532}, \delta_{1064}$). The particle
113 depolarization ratio, determined as a ratio of cross- and co-polarized components of the particle
114 backscattering coefficient, was calculated and calibrated in the same way as described in
115 Freudenthaler et al. (2009). The aerosol extinction and backscattering coefficients at 355 and 532
116 nm were calculated from Mie-Raman observations (Ansmann et al., 1992), while β_{1064} was
117 derived by the Klett method (Fernald, 1984; Klett, 1985). Additional information about
118 atmospheric parameters was available from radiosonde measurements performed at
119 Herstmonceux (UK) and Beauvechain (Belgium) stations, located 160 km and 80 km away
120 from the observation site respectively.

121 This lidar system is also capable to perform aerosol fluorescence measurements. A part of
122 the fluorescence spectrum is selected by a wideband interference filter of 44 nm width centered
123 at 466 nm (Veselovskii et al., 2020; 2021). The strong sunlight background at daytime restricts
124 the fluorescence observations to nighttime hours. To characterize the fluorescence properties of

125 aerosol, the fluorescence backscattering coefficient β_F is calculated from the ratio of
126 fluorescence and nitrogen Raman backscatters, as described in Veselovskii et al. (2020). This
127 approach allows to evaluate the absolute values of β_F , if the relative sensitivity of the channels is
128 calibrated and the nitrogen Raman scattering differential cross section σ_R is known. In our
129 research we used $\sigma_R=2.744*10^{-30}$ cm²sr⁻¹ at 355 nm from Venable et al. (2011). All β_F profiles
130 presented in this work were smoothed with the Savitzky – Golay method, using second order
131 polynomial with 21 points in the window. The efficiency of fluorescence backscattering with
132 respect to elastic backscattering β_{532} is characterized by the fluorescence capacity $G_F = \frac{\beta_F}{\beta_{532}}$.

133 For most of atmospheric particles β_F is proportional to the volume of dry matter, while
134 dependence of β_{532} on particle size is more complicated. As a result, G_F depends not only on
135 aerosol type, but also on particle size and the relative humidity RH. Uncertainty of β_F calculation
136 depends on the chosen value of σ_R and on relative transmission of optical elements in
137 fluorescence and nitrogen channels. These system parameters do not change with time. The
138 relative sensitivity of PMTs, however, may change. Regular calibration of the channels relative
139 sensitivity (Veselovskii et al., 2020), demonstrates that corresponding uncertainty can be up to
140 10%. At high altitudes the statistical uncertainty becomes predominant. We recall also, that only
141 a part of the fluorescence spectra was selected by the interference filter in the receiver, so
142 provided values of β_F and G_F are specific for the filter used. Analyzing the fluorescence
143 measurements we should keep in mind, that the sensitivity of this technique can be limited by the
144 fluorescence of optics in the lidar receiver. The minimal value of G_F , which we measured during
145 observation in cloudy conditions in the lower troposphere was about 2×10^{-8} . Thus, at least, in the
146 measurements with G_F above this value, the contribution of optics fluorescence can be ignored.

147

148 **3. Results of the measurements**

149 ***3.1. Observation of smoke particles in UTLS***

150 Smoke particles produced by intensive fires and transported across the Atlantic are
151 regularly observed in the UTLS height range over Europe (Müller et al., 2005; Hu et al., 2019;
152 Baars et al., 2019, 2021). One of such events, observed over Lille in the night of 4-5 November
153 2020, is shown in Fig.1. The figure provides height – time displays of the range corrected lidar
154 signal and the volume depolarization ratio at 1064 nm together with the fluorescence

155 backscattering coefficient. A narrow smoke layer occurred in the upper troposphere in the period
156 from 23:00 – 06:00 UTC. The smoke was detected at heights above 12 km after midnight. The
157 particles caused a low volume depolarization ratio (<5%) at 1064 nm and strong fluorescence
158 backscattering ($\beta_F > 1.2 \times 10^{-4} \text{ Mm}^{-1} \text{sr}^{-1}$). The backward trajectory analysis indicated that the
159 aerosol layer was transported over the Atlantic and contained products of North American wild
160 fires.

161 Vertical profiles of aerosol β_{532} and fluorescence β_F backscattering coefficients for the
162 period from 02:00 - 05:30 UTC are shown in Fig.2a. The fluorescence capacity G_F in the center
163 of smoke layer (not shown) was about 4.5×10^{-4} . The depolarization ratio of aged smoke in the
164 UTLS height range usually shows a strong spectral dependence (Haarig et al., 2018; Hu et al.,
165 2019). For the case presented in Fig.2a the particle depolarization ratio in the center of the smoke
166 layer decreased from $16 \pm 4\%$ at 355 nm (δ_{355}) to $4 \pm 1\%$ at 1064 (δ_{1064}). The tropopause height H_{tr}
167 was at about 13000 m, thus the main part of the smoke layer was below the tropopause. By the
168 end of day the smoke layer became weaker ($\beta_F < 0.3 \times 10^{-4} \text{ Mm}^{-1} \text{sr}^{-1}$) and ascended up to 14500 m,
169 which is above the tropopause. The corresponding vertical profiles of β_{532} and β_F are shown in
170 Fig.2b. The fluorescence capacity in the center of the layer is about 4.5×10^{-4} , which is close to
171 the value observed during 02:00 - 05:30 UTC period.

172 An important advantages of the fluorescence lidar technique is the ability to monitor
173 smoke particles inside cirrus clouds. The results of smoke observations in the presence of ice
174 clouds are shown in Fig.3. Cirrus clouds occurred during the whole night in the height range
175 from 6.0 km – 10.0 km. To quantify the fluorescence backscattering inside the cloud (which was
176 rather weak in this case), the lidar signals were averaged over the full 18:00 – 06:00 UTC time
177 interval in Fig.3a. The fluorescence backscatter coefficient shown in Fig.3c decreased from
178 $\beta_F = 0.015 \times 10^{-4} \text{ Mm}^{-1} \text{sr}^{-1}$ at 5000 m (near the cloud base) to a minimum value of $0.01 \times 10^{-4} \text{ Mm}^{-1} \text{sr}^{-1}$
179 at 7000 m inside the cirrus layer. Above the tropopause the fluorescence backscattering
180 increased strongly and reached the maximum (about $0.3 \times 10^{-4} \text{ Mm}^{-1} \text{sr}^{-1}$) in 11000 m -13000 m
181 height.

182 The analysis of fluorescence measurements performed during strong smoke episodes in
183 the summer and autumn of 2020, when smoke layers from North American fires frequently
184 reached Europe, demonstrates that the fluorescence capacity varied within the range of 2.5×10^{-4}
185 to 4.5×10^{-4} . The variations are a function of smoke composition, relative humidity and particle

186 size. However, in the upper troposphere, where relative humidity is low, G_F was normally close
 187 to 4.5×10^{-4} . This relatively low range of G_F variations allows the estimation of the backscattering
 188 coefficient attributed to the smoke particles from fluorescence measurements as:

$$189 \quad \beta_{532}^s = \frac{\beta_F}{G_F}. \quad (1)$$

190 Fig.3d shows the smoke backscattering coefficient β_{532}^s , calculated from β_F for
 191 $G_F=4.5 \times 10^{-4}$, together with β_{532} . The dynamical range of β_{532} variations is high. To make smoke
 192 backscattering visible above H_{Tr} , β_{532} is plotted in expanded scale in Fig.3d. The β_{532}^s values,
 193 though being strongly oscillating above the tropopause, match the β_{532} indicating that the smoke
 194 contribution to backscattering was predominant.

195

196 3.2. Estimation of smoke particles content based on fluorescence measurements

197 The possibility to detect fluorescence backscattering inside the cirrus clouds reveals also
 198 the opportunity for a quantitative characterization of the smoke content. This can be realized by a
 199 synergistic use of fluorescence and multiwavelength Mie – Raman lidar observations. The flow
 200 chart, summarizing the main steps of this procedure, is presented in **Appendix 1**. For the smoke
 201 layers with sufficient optical depth, the number N , surface area S and volume V concentrations
 202 can be evaluated, by inverting the $3\beta+2\alpha$ observations consisting of three backscatter
 203 coefficients (355, 532, 1064 nm) and two extinction coefficients (355, 532 nm) (Müller et al.,
 204 1999; Veselovskii et al., 2002; Pérez-Ramírez et al., 2013). The conversion factors C_N , C_S , C_V ,
 205 introduced as

$$206 \quad C_N = \frac{N}{\beta_F}, \quad C_S = \frac{S}{\beta_F}, \quad C_V = \frac{V}{\beta_F}, \quad (3)$$

207 allow the estimation of smoke particle concentration inside the clouds from fluorescence
 208 backscattering, assuming that smoke contribution to the fluorescence is predominant. Moreover,
 209 it allows estimation of the particles concentration in weak smoke layers in UTLS, where $3\beta+2\alpha$
 210 observations are normally not available.

211 On 23-24 June 2020, a strong smoke layer was observed in 4500 – 5500 m height during
 212 the whole night (Fig.4). The vertical profiles of the aerosol backscattering and extinction
 213 coefficients ($3\beta+2\alpha$) are shown in Fig.5a, while the particle depolarization ratios δ_{355} , δ_{532} , δ_{1064}

214 and the lidar ratios at 355 nm and 532 nm (LR_{355} , LR_{532}) are presented in Fig.5b. The
 215 depolarization ratio decreases with wavelength from $9\pm1.5\%$ at 355 nm to $1.5\pm0.3\%$ at 1064 nm
 216 and the lidar ratio at 532 nm significantly exceeds corresponding value at 355 nm (80 ± 12 sr and
 217 50 ± 7.5 sr respectively), which is typical for aged smoke (Müller et al., 2005). The
 218 multiwavelength observations were inverted to determine the particle effective radius r_{eff} ,
 219 number, surface area and volume concentrations for seven height bins inside the smoke layer.
 220 The effective radius r_{eff} in Fig.5c increases through the layer from $0.15\text{ }\mu\text{m}$ to $0.2\text{ }\mu\text{m}$
 221 simultaneously with the increase of the fluorescence capacity G_F from 2.8×10^{-4} to 3.6×10^{-4} .
 222 Retrieved values of N , S , V were used for the calculation of the conversion factors (Eq. 3) for
 223 each height bin. In the center of the smoke layer (at 4.9 km) the factors are: $C_N=88\times10^4$
 224 $\frac{cm^{-3}}{Mm^{-1}sr^{-1}}$, $C_S=35\times10^4\frac{\mu m^2cm^{-3}}{Mm^{-1}sr^{-1}}$, and $C_V=2.4\times10^4\frac{\mu m^3cm^{-3}}{Mm^{-1}sr^{-1}}$. Thus, when β_F is given in $Mm^{-1}sr^{-1}$,
 225 the calculated values of N , S , and V are given in cm^{-3} , μm^2cm^{-3} and μm^3cm^{-3} respectively.
 226 Fluorescence backscattering is proportional to the particle volume concentration, so C_V is not
 227 sensitive to the effective radius variation. The conversion factors C_N and C_S , on the contrary,
 228 depend on the particle size. Fig.5d shows the profiles of N , S , V obtained by inversion of $3\beta+2\alpha$
 229 observations (symbols) together with corresponding values (N^S , S^S , V^S) obtained from β_F , using
 230 the mean conversion factors for seven height bins considered. The volume concentrations V and
 231 V^S agree well for all seven height bins. For the surface area concentrations the agreement is still
 232 good, but for N and N^S the difference is up to 30%. We need to emphasize, that the conversion
 233 factors presented are specific for our lidar system (for the interference filter installed in
 234 fluorescence channel). It is worthwhile to mention that the ratio V/α_{532} of the volume
 235 concentration V in Fig.5d to the extinction coefficient α at 532 nm in Fig.5a, as well as the ratio
 236 S/α_{532} , are very close to respective extinction-to-volume and extinction-to-surface-area-
 237 concentration conversion factors presented for aged wildfire smoke by Ansmann et al. (2021).

238 The conversion factors depend on the smoke composition. To estimate the variation range
 239 of C_N , C_S , C_V , several smoke episodes were analyzed and corresponding results are presented in
 240 Table 1. The table provides the fluorescence capacity G_F and the conversion factors at the
 241 heights, where $3\beta+2\alpha$ data could be calculated. Mean values of $\langle C_N \rangle$, $\langle C_S \rangle$, $\langle C_V \rangle$ derived for
 242 these episodes and corresponding standard deviations are:

243 $\langle C_N \rangle = (61 \pm 32) \times 10^4 \frac{\text{cm}^{-3}}{\text{Mm}^{-1} \text{sr}^{-1}}$; $\langle C_S \rangle = (28 \pm 6.4) \times 10^4 \frac{\mu\text{m}^2 \text{cm}^{-3}}{\text{Mm}^{-1} \text{sr}^{-1}}$; $\langle C_V \rangle = (2.2 \pm 0.2) \times 10^4 \frac{\mu\text{m}^3 \text{cm}^{-3}}{\text{Mm}^{-1} \text{sr}^{-1}}$ (4)

244 Table 1 shows also the volume and surface area concentrations of the smoke particles obtained
 245 from the inversion of $3\beta+2\alpha$ observations (V, S) and calculated from β_F (V^S, S^S) using the
 246 conversion factors in Eq. (4). Standard deviations of V^S and S^S from corresponding values of
 247 $V_{3\beta+2\alpha}$ and $S_{3\beta+2\alpha}$ are 10% and 25% respectively.

248 The mean conversion factors in Eq. (4) are now used to estimate the smoke
 249 microphysical properties inside the cloud, assuming in addition that the predominant contribution
 250 to the fluorescence is provided by the smoke. Table 2 summarizes the number, surface area, and
 251 volume concentrations of smoke particles inside the ice clouds, estimated from fluorescence
 252 measurements for four episodes considered in this paper. On September 12-13, 2020, the smoke
 253 layer with high fluorescence and low depolarization ratio at 1064 nm (below 4%) was observed
 254 during the whole night inside the 2.0 km – 5.0 km height range. The cirrus cloud occurred above
 255 11000 m also during the whole night. Fig.6a presents vertical profiles of the aerosol β_{532} and
 256 fluorescence β_F backscattering coefficients. Fluorescence backscattering shows a maximum at
 257 3.5 km, but it is detected even inside the cloud. The smoke backscattering coefficient β_{532}^S ,
 258 computed from β_F for $G_F=3.6 \times 10^{-4}$ agrees well with β_{532} inside the 2.0 – 10.0 km height range
 259 (Fig.6b). The height profile of the surface area concentration of the smoke particles S^S , calculated
 260 from β_F using the respective conversion factor in Eq. (4), is shown in Fig.6c. In the smoke layer,
 261 S^S is up to $60 \mu\text{m}^2/\text{cm}^3$, while in the center of the cloud in 12 km – 13 km height the average
 262 value of S^S is $1.6 \pm 0.4 \mu\text{m}^2/\text{cm}^3$. Corresponding values of number and volume concentrations in
 263 the cloud center are $3.5 \pm 1.8 \text{ cm}^{-3}$ and $0.13 \pm 0.013 \mu\text{m}^3/\text{cm}^3$.

264 The temperature in the cloud ranged from about -50°C to almost -70°C and was -68°C at
 265 cirrus top in Fig.6b where ice nucleation usually starts. We applied the immersion freezing INP
 266 parameterization of Knopf and Alpert (2013) for Leonardite (a standard humic acid surrogate
 267 material) and assume that this humic compound represents the amorphous organic coating of
 268 smoke particles. The INP parameterization for smoke particles is summarized for lidar
 269 applications in Ansmann et al. (2021). The selected parameterization allows the estimation of the
 270 INP concentration as a function of ambient air temperature (freezing temperature), ice
 271 supersaturation, particle surface area, and time period for which a certain level of ice
 272 supersaturation is given. We simply assume a constant ice supersaturation of around 1.45 during

273 a time period of 600 s (upwind phase of a typical gravity wave in the upper troposphere). The
274 temperature at cirrus top height is set to -68°C and the aerosol surface area concentration to 2.0
275 $\mu\text{m}^2/\text{cm}^3$ as indicated in Fig.6c. The obtained INP concentrations of $1\text{-}10 \text{ L}^{-1}$ for these
276 meteorological and aerosol environmental conditions can be regarded as the predicted number
277 concentration of ice crystals nucleated in the cirrus top region. Ice crystal number concentration
278 of $1\text{-}10 \text{ L}^{-1}$ are typical values in cirrus layers when heterogeneous ice nucleation dominates
279 (typical values of INP concentrations and supersaturation are discussed e.g. in Sullivan et al,
280 (2016), Ansmann et al. (2019; 2021), Engelmann et al. (2021)). It should be mentioned that the
281 required very high ice supersaturation levels of close to 1.5 (ice supersaturation of 1.1-1.2 is
282 sufficient in case of mineral dust particles) are still lower than the threshold supersaturation level
283 of >1.5 at which homogeneous freezing starts to dominate. At low updraft velocities around 10-
284 25 cm/s, as usually given in gravity waves in the upper troposphere (Barahona et al., 2017),
285 heterogeneous ice nucleation very likely dominates the ice production when cirrus evolves in
286 detected aerosol layers.

287

288 **3.3. Ice formation inside the smoke layers.**

289 During September 2020 we observed several episodes with ice cloud formation inside of
290 smoke layers. One of such episodes occurred on 11-12 September 2020 and is shown in Fig.7.
291 The height – time display of the fluorescence backscattering coefficient reveals the smoke layer
292 in the 5.0 - 10.0 km height range. Inside this layer, we can observe a short time interval of 15
293 minutes with a strongly increased depolarization ratio around 10.5 km height (red spots),
294 indicating ice cloud formation. Fig.8 shows vertical profiles of the aerosol backscattering
295 coefficients β_{355} , β_{532} , and β_{1064} as well the particle depolarization ratios δ_{355} , δ_{532} , and δ_{1064} for
296 two temporal intervals. The first interval (23:00 – 00:30 UTC) is prior to ice cloud formation and
297 the second one (01:20 – 01:45 UTC) covers ice occurrence period. The depolarization ratios at
298 all three wavelengths were $< 5\%$ below 6 km height. Above that height δ_{355} significantly
299 increased reaching the value of 10% at 7 km (Fig.8b), which is indicative of a change of the
300 particle shape (from spherical to irregular shape). The fluorescence capacity also changed with
301 height, being about $G_F=4.5\times10^{-4}$ at 5.5 km and it decreases to 3.5×10^{-4} by 8 km. The profile of
302 β_{532}^s shown in Fig.8c is calculated assuming $G_F=4.0\times10^{-4}$ and it matches well the profile of β_{532}
303 for the whole height range. The aerosol layer at 10.5 km is thus a pure smoke layer. Ice

304 formation at 10.5 km (Fig.8d-f) leads to a significant increase of β_{532} while β_{532}^s (or the
305 respective fluorescence backscatter coefficient β_F) remains low and at the same level as observed
306 below the cirrus layer, i.e., below 10 km height. The depolarization ratios at all three
307 wavelengths increases to typical cirrus values around 40%. The temperature at 10.5 km is about -
308 50 °C, and the surface area concentration of the smoke particles inside the cloud, estimated from
309 β_F , is about $10 \mu\text{m}^2/\text{cm}^3$ (see Fig.8f, thin blue line). For these temperature and aerosol conditions
310 we yield smoke INP concentrations of $1-10 \text{ L}^{-1}$ for ice supersaturation values even below 1.4
311 (1.38-1.4) and updraft duration of 600 s. When comparing Fig.8c and 8f at cirrus level it seems
312 to be that ice nucleation on the smoke particles widely depleted the smoke INP reservoir.

313 Another case of ice formation in the smoke layer was observed on 17-18 September
314 2020. Strong smoke layers occurred in the 5.0 km – 9.0 km height range as shown in Fig.9.
315 During the period from 22:30 – 00:00 UTC, the depolarization increased at 8.5 km height,
316 indicating ice formation. Vertical profiles of the particle parameters prior and during ice
317 formation are shown in Fig.10. The β_{532}^s calculated for $G_F=3.5\times10^{-4}$ matches well with β_{532}
318 below 6.9 km and above 8.0 km (Fig.10c), but inside the 7.0 km – 8.0 km height range
319 $\beta_{532} > \beta_{532}^s$, meaning that G_F was decreased. The depolarization ratio in the 7.0 km – 8.0 km
320 height range shows some enhancement (Fig.10b): in particular, δ_{532} increased from 10% to 12%.
321 Cloud formation at 8.5 km (Fig.10d) led to a significantly smaller increase of the depolarization
322 ratio, compared to the case on 11-12 September. Prior to the cloud formation the values of δ_{1064} ,
323 δ_{532} , and δ_{355} at 8.5 km were of 3%, 10%, and 13% respectively (Fig.10b) and in the cloud
324 corresponding depolarization ratios increase up to 9%, 15%, 20%. The reason is probably that
325 the signal averaging period from 22:45 to 23:45 UTC includes cloud-free section. Three gravity
326 waves obviously crossed the lidar field site and triggered ice nucleation just before 23 UTC, 15-
327 30 minutes after 23 UTC, and around mid night (00:00 UTC). The temperature at cloud top at
328 about 8.5-8.6 km height was close to -35°C. For this high temperature and the high particle
329 surface area concentration of $200 \mu\text{m}^2/\text{cm}^3$ (see Fig.10d, thin blue line) we yield smoke INP
330 concentrations of $1-10 \text{ L}^{-1}$ for a relatively low ice supersaturation of 1.30-1.33 and an updraft
331 period of 600 s. Again, a depletion of the INP reservoir is visible after formation of the cirrus
332 layer (see Figs.6c and 6d around and above 8.5 km height).

333

334 **Conclusion**

335 The operation of a fluorescence channel in the LILAS lidar during strong smoke events in
336 the summer and autumn seasons of 2020 has demonstrated the ability of the fluorescence lidar
337 technique to discriminate ice from smoke particles in atmospheric layers in the UTLS height
338 range in large detail. The fluorescence capacity G_F of smoke particles during this period varied
339 within a relatively small range: $2.5\text{--}4.5 \times 10^{-4}$, thus the use of the mean value of G_F allows to
340 estimate the contribution of smoke to the total particle backscattering coefficient. The
341 fluorescence lidar technique makes it possible to estimate smoke parameters, such as number,
342 surface area and volume concentration in UTLS height range in a quantitative way by applying
343 conversion factors (C_N , C_S , C_V) which link the fluorescence backscattering and the smoke
344 microphysical properties. These factors, derived from the synergy of multiwavelength Mie-
345 Raman and fluorescence lidar observations, show some variation from episode to episode,
346 however, the use of mean values $\langle C_N \rangle$, $\langle C_S \rangle$, $\langle C_V \rangle$ allows estimation of smoke properties in
347 UTLS height regime with reasonable accuracy. Based on two case studies, we demonstrated that
348 the fluorescence lidar technique provides the unique possibility to characterize the smoke
349 particles and their amount inside cirrus cloud layers. The smoke input parameter (surface area
350 concentration) in smoke INP parameterization schemes that are used to predict ice crystal
351 number concentrations in cirrus generation cells, can now be estimated within freshly formed
352 cirrus layers.

353 The smoke parameters such as fluorescence capacity and conversion factors were derived
354 from observations of aged wildfire smoke, transported over Atlantic in 2020. However, smoke
355 composition, depends on many factors, such as burning materials type, flame temperature and
356 environmental conditions, thus the smoke fluorescence properties may also vary. Hence, it is
357 important to perform the measurements for different locations and seasons. The fluorescence
358 backscattering in UTLS height range is quite weak, so to perform measurements with higher
359 temporal resolution more powerful lidar systems are needed. A dedicated high power Lidar,
360 LIFE (Laser Induced Fluorescence Explorer), will be designed and operated at ATOLL, in the
361 frame of OBS4CLIM/ACTRIS-France .

362

363 **Data availability.** Lidar measurements are available upon request
364 (philippe.goloub@univ-lille.fr).
365

366 **Author contributions.** IV processed the data and wrote the paper. QH and TP performed the
367 measurements. A.A. analyzed results of fluorescence measurements and ice formation in smoke
368 layers. PG supervised the project and helped with paper preparation. MK developed software for
369 data processing.

370 .

371 **Competing interests.** The authors declare that they have no conflict of interests.

372

373

374 **Acknowledgement**

375 We acknowledge funding from the CaPPA project funded by the ANR through the PIA under
376 contract ANR-11-LABX-0005-01, the “Hauts de France” Regional Council (project CLIMIBIO)
377 and the European Regional Development Fund (FEDER). Development of algorithm for analysis
378 of fluorescence observations was supported by Russian Science Foundation (project 21-17-
379 00114). ESA/QA4EO program is greatly acknowledged for support of observation activity at
380 LOA.

381

382 **References**

383 Ansmann, A., Riebesell, M., Wandinger, U., Weitkamp, C., Voss, E., Lahmann, W., and
384 Michaelis, W.: Combined Raman elastic-backscatter lidar for vertical profiling of moisture,
385 aerosols extinction, backscatter, and lidar ratio, *Appl.Phys.B*, 55, 18-28, 1992.

386 Ansmann, A., Baars, H., Chudnovsky, A., Mattis, I., Veselovskii, I., Haarig, M., Seifert, P.,
387 Engelmann, R., and Wandinger, U.: Extreme levels of Canadian wildfire smoke in the
388 stratosphere over central Europe on 21–22 August 2017, *Atmos. Chem. Phys.*, 18, 11831–
389 11845, 2018. <https://doi.org/10.5194/acp-18-11831-2018>.

390 Ansmann, A., Mamouri, R.-E., Hofer, J., Baars, H., Althausen, D., and Abdullaev, S. F.: Dust
391 mass, cloud condensation nuclei, and ice-nucleating particle profiling with polarization lidar:
392 updated POLIPHON conversion factors from global AERONET analysis, *Atmos. Meas.
393 Tech.*, 12, 4849–4865, <https://doi.org/10.5194/amt-12-4849-2019>, 2019a.

394 Ansmann, A., Mamouri, R.-E., Bühl, J., Seifert, P., Engelmann, R., Hofer, J., Nisantzi, A.,
395 Atkinson, J. D., Kanji, Z. A., Sierau, B., Vrekoussis, M., and Sciare, J.: Ice-nucleating particle
396 versus ice crystal number concentrationin altocumulus and cirrus layers embedded in Saharan

397 dust:a closure study, *Atmos. Chem. Phys.*, 19, 15087–15115, <https://doi.org/10.5194/acp-19-15087-2019>, 2019b.

399 Ansmann, A., Ohneiser, K., Mamouri, R.-E., Veselovskii, I., Knopf, D. A., Baars, H.,
400 Engelmann, R., Foth, A., Jimenez, C., Seifert, P., and Barja, B.: Tropospheric and
401 stratospheric wildfire smoke profiling with lidar: Mass, surface area, CCN and INP retrieval,
402 *Atmos. Chem. Phys.*, 21, 9779–9807, 2021. <https://doi.org/10.5194/acp-21-9779-2021>.

403 Baars, H., Ansmann, A., Ohneiser, K., Haarig, M., Engelmann, R., Althausen, D., Hanssen, I.,
404 Gausa, M., Pietruczuk, A., Szkop, A., Stachlewska, I. S., Wang, D., Reichardt, J., Skupin, A.,
405 Mattis, I., Trickl, T., Vogelmann, H., Navas-Guzmán, F., Haefele, A., Acheson, K., Ruth, A.
406 A., Tatarov, B., Müller, D., Hu, Q., Podvin, T., Goloub, P., Veselovskii, I., Pietras, C.,
407 Haeffelin, M., Fréville, P., Sicard, M., Comerón, A., Fernández García, A. J., Molero
408 Menéndez, F., Córdoba-Jabonero, C., Guerrero-Rascado, J. L., Alados-Arboledas, L., Bortoli,
409 D., Costa, M. J., Dionisi, D., Liberti, G. L., Wang, X., Sannino, A., Papagiannopoulos, N.,
410 Boselli, A., Mona, L., D'Amico, G., Romano, S., Perrone, M. R., Belegante, L., Nicolae, D.,
411 Grigorov, I., Gialitaki, A., Amiridis, V., Soupiona, O., Papayannis, A., Mamouri, R.-E.,
412 Nisantzi, A., Heese, B., Hofer, J., Schechner, Y. Y., Wandinger, U., and Pappalardo, G.: The
413 unprecedented 2017–2018 stratospheric smoke event: decay phase and aerosol properties
414 observed with the EARLINET, *Atmos. Chem. Phys.*, 19, 15183–15198,
415 <https://doi.org/10.5194/acp-19-15183-2019>, 2019.

416 Baars, H., Radenz, M., Floutsi, A. A., Engelmann, R., Althausen, D., Heese, B., Ansmann, A.,
417 Flament, T., Dabas, A., Trapon, D., Reitebuch, O., Bley, S., and Wandinger, U.: Californian
418 wildfire smoke over Europe: A first example of the aerosol observing capabilities of Aeolus
419 compared to ground-based lidar. *Geophysical Research Letters*, 48, e2020GL092194.
420 <https://doi.org/10.1029/2020GL092194>, 2021.

421 Barahona, D., Molod, A., and Kalesse, H.: Direct estimation of the global distribution of vertical
422 velocity within cirrus clouds, *Sci. Rep.*, 7, 20 6840, <https://doi.org/10.1038/s41598-017-07038-6>, 2017.

424 Boose, Y., Sierau, B., Garcia, M. I., Rodriguez, S., Alastuey, A., Linke, C., Schnaiter, M.,
425 Kupiszewski, P., Kanji, Z. A., and Lohmann, U.: Ice nucleating particles in the Saharan Air
426 Layer, *Atmos. Chem. Phys.*, 16, 9067–9087, <https://doi.org/10.5194/acp-16-9067-2016>, 2016.

427 China, S., Alpert, P. A., Zhang, B., Schum, S., Dzepina, K., Wright, K., Owen, R. C., Fialho, P.,
428 Mazzoleni, L. R., Mazzoleni, C., and Knopf, D. A.: Ice cloud formation potential by free
429 tropospheric particles from long-range transport over the Northern Atlantic Ocean, *J.
430 Geophys. Res.-Atmos.*, 122, 3065–3079, <https://doi.org/10.1002/2016JD025817>, 2017.

431 DeMott, P. J., Prenni, A. J., Liu, X., Kreidenweis, S. M., Petters, M. D., Twohy, C. H.,
432 Richardson, M. S., Eidhammer, T., and Rogers, D. C.: Predicting global atmospheric ice
433 nuclei distributions and their impacts on climate, *Proc. Natl. Acad. Sci. USA*, 107, 11217–
434 11222, doi:10.1073/pnas.0910818107, 2010.

435 DeMott, P. J., Prenni, A. J., McMeeking, G. R., Sullivan, R. C., Petters, M. D., Tobo, Y.,
436 Niemand, M., Möhler, O., Snider, J. R., Wang, Z., and Kreidenweis, S. M.: Integrating
437 laboratory and field data to quantify the immersion freezing ice nucleation activity of mineral
438 dust particles, *Atmos. Chem. Phys.*, 15, 393–409, doi:10.5194/acp-15-393-2015, 2015.

439 Engelmann, R., Ansmann, A., Ohneiser, K., Griesche, H., Radenz, M., Hofer, J., Althausen, D.,
440 Dahlke, S., Maturilli, M., Veselovskii, I., Jimenez, C., Wiesen, R., Baars, H., Bühl, J.,
441 Gebauer, H., Haarig, M., Seifert, P., Wandinger, U., and Macke, A.: Wildfire smoke, Arctic
442 haze, and aerosol effects on mixed-phase and cirrus clouds over the North Pole region during
443 MOSAiC: an introduction, *Atmos. Chem. Phys.*, 21, 13397–13423,
444 <https://doi.org/10.5194/acp-21-13397-2021>, 2021.

445 Fernald, F. G.: Analysis of atmospheric lidar observations: some comments, *Appl. Opt.*, 23, 652–
446 653, doi.org/10.1364/AO.23.000652, 1984.

447 Freudenthaler, V., Esselborn, M., Wiegner, M., Heese, B., Tesche, M. and co-authors:
448 Depolarization ratio profiling at several wavelengths in pure Saharan dust during SAMUM
449 2006, *Tellus* 61B, 165–179, 2009.

450 Fromm, M., Lindsey, D. T., Servranckx, R., Yue, G., Trickl, T., Sica, R., Doucet, P., and Godin-
451 Beekmann, S. E.: The untold story of pyrocumulonimbus, *B. Am. Meteorol. Soc.*, 91, 1193–
452 1209, <https://doi.org/10.1175/2010bams3004.1>, 2010.

453 Grawe, S., Augustin-Bauditz, S., Hartmann, S., Hellner, L., Pettersson, J. B. C., Prager, A.,
454 Stratmann, F., and Wex, H.: The immersion freezing behavior of ash particles from wood and
455 brown coal burning, *Atmospheric Chemistry and Physics*, 16, 13 911–13 928, 2016.
456 <https://doi.org/10.5194/acp-16-13911-2016>.

457 Haarig, M., Ansmann, A., Baars, H., Jimenez, C., Veselovskii, I., Engelmann, R., and Althausen,
458 D.: Depolarization and lidar ratios at 355, 532, and 1064 nm and microphysical properties of
459 aged tropospheric and stratospheric Canadian wildfire smoke, *Atmos. Chem. Phys.*, 18,
460 11847-11861, <https://doi.org/10.5194/acp-18-11847-2018>, 2018.

461 Holben, B. N., Eck, T. F., Slutsker, I., Tanré, D., Buis, J. P., Setzer, A., Vermote, E., Reagan, J.
462 A., Kaufman, Y. J., Nakajima, T., Lavenu, F., Jankowiak, I., and Smirnov, A.: AERONET – a
463 federated instrument network and data archive for aerosol characterization, *Remote Sens.*
464 *Environ.*, 66, 1–16, 1998.

465 Hoose, C. and Möhler, O.: Heterogeneous ice nucleation on atmospheric aerosols: a review of
466 results from laboratory experiments. *Atmos. Chem. Phys.*, 12, 9817–9854, 2012.
467 doi:10.5194/acp-12-9817-2012

468 Hu, Q., Goloub, P., Veselovskii, I., Bravo-Aranda, J.-A., Popovici, I. E., Podvin, T., Haeffelin,
469 M., Lopatin, A., Dubovik, O., Pietras, C., Huang, X., Torres, B., and Chen, C.: Long-range-
470 transported Canadian smoke plumes in the lower stratosphere over northern France, *Atmos.*
471 *Chem. Phys.*, 19, 1173-1193, 2019. <https://doi.org/10.5194/acp-19-1173-2019>.

472 Jahl, L. G., Brubaker, T. A., Polen, M. J., Jahn, L. G., Cain, K. P., Bowers, B. B., Fahy, W. D.,
473 Graves, S., and Sullivan, R. C.: Atmospheric aging enhances the ice nucleation ability of
474 biomass-burning aerosol, *Science Advances*, 7, eabd3440, 2021.

475 Kanji, Z. A., Ladino, L. A., Wex, H., Boose, Y., Burkert-Kohn, M., Cziczo, D. J., and Krämer,
476 M.: Chapter 1: Overview of ice nucleating particles, *Meteor Monogr.*, Am. Meteorol. Soc.,
477 58, 1.1-1.33, <https://doi.org/10.1175/amsmonographs-d-16-0006.1>, 2017.

478 Khaykin, S., Legras, B., Bucci, S., Sellitto, P., Isaksen, L., Tencé, F., Bekki, S., Bourassa, A.,
479 Rieger, L., Tawada, D., Jumelet, J., and Godin-Beekmann, S.: The 2019/20 Australian
480 wildfires generated a persistent smoke-charged vortex rising up to 35 km altitude, *Commun.*
481 *Earth Environ.*, 1, 22, <https://doi.org/10.1038/s43247-020-00022-5>, 2020.

482 Klett J.D., “Lidar inversion with variable backscatter/extinction ratios”, *Appl. Opt.* 24, 1638-
483 1643, 1985.

484 Knopf, D. A., Alpert, P. A., and Wang, B.: The role of organic aerosol in atmospheric ice
485 nucleation: a review, *ACS Earth and Space Chemistry*, 2, 168–202, 2018.

486 Müller, D., Wandinger, U., and Ansmann, A.: Microphysical particle parameters from extinction
487 and backscatter lidar data by inversion with regularization: theory, *Appl. Opt.* 38, 2346-2357,
488 1999.

489 Müller, D., Mattis, I., Wandinger, U., Ansmann, A., Althausen, A., and Stohl, A.: Raman lidar
490 observations of aged Siberian and Canadian forest fire smoke in the free troposphere over
491 Germany in 2003: Microphysical particle characterization, *J. Geophys. Res.*, 110, D17201,
492 doi:10.1029/2004JD005756, 2005.

493 Murray, B. J., O'Sullivan, D., Atkinson, J. D., and Webb, M. E.: Ice nucleation by particles
494 immersed in supercooled cloud droplets, *Chem. Soc. Rev.*, 41, 6519–6554,
495 <https://doi.org/10.1039/c2cs35200a>, 2012.

496 Ohneiser, K., Ansmann, A., Engelmann, R., Ritter, C., Chudnovsky, A., Veselovskii, I., Baars,
497 H., Gebauer, H., Griesche, H., Radenz, M., Hofer, J., Althausen, D., Dahlke, S., and Maturilli,
498 M.: Siberian fire smoke in the High-Arctic winter stratosphere observed during MOSAiC
499 2019–2020, *Atmos. Chem. Phys. Discuss. [preprint]*, <https://doi.org/10.5194/acp-2021-117>, in
500 review, 2021.

501 Peterson, D. A., Campbell, J. R., Hyer, E. J., Fromm, M. D., Kablick, G. P., Cossuth, J. H., and
502 DeLand, M. T.: Wildfire-driven thunderstorms cause a volcano-like stratospheric injection of
503 smoke, *npj Clim. Atmos. Sci.*, 1, 30, <https://doi.org/10.1038/s41612-018-0039-3>, 2018

504 Pérez-Ramírez, D., Whiteman, D. N., Veselovskii, I., Kolgotin, A., Korenskiy, M., and
505 Alados-Arboledas, L.: Effects of systematic and random errors on the retrieval of particle
506 microphysical properties from multiwavelength lidar measurements using inversion with
507 regularization, *Atmos. Meas. Tech.*, 6, 3039-3054, 2013.

508 Prata, A.T., Young, S.A., Siems S.T., and Manton, M.J.: Lidar ratios of stratospheric volcanic
509 ash and sulfate aerosols retrieved from CALIOP measurements *Atmos. Chem. Phys.*, 17,
510 8599–8618, 2017. <https://doi.org/10.5194/acp-17-8599-2017>

511 Reichardt, J., Leinweber, R., Schwebe, A.: Fluorescing aerosols and clouds: investigations of co-
512 existence, *Proceedings of the 28th ILRC*, Bucharest, Romania, 25-30 June, 2017.

513 Richardson, S.C., Mytilinaios, M., Foskinis, R., Kyrou, C., Papayannis, A., Pyrri, I.,
514 Giannoutsou, E., Adamakis, I.D.S.: Bioaerosol detection over Athens, Greece using the laser
515 induced fluorescence technique, *Science of the Total Environment* 696, 133906, 2019.
516 <https://doi.org/10.1016/j.scitotenv.2019.133906>

517 Schrod, J., Weber, D., Drücke, J., Keleshis, C., Pikridas, 5 M., Ebert, M., Cvetkovic', B.,
518 Nickovic, S., Marinou, E., Baars, H., Ansmann, A., Vrekoussis, M., Mihalopoulos, N., Sciare,
519 J., Curtius, J., and Bingemer, H. G.: Ice nucleating particles over the Eastern Mediterranean
520 measured by unmanned aircraft systems, *Atmos. Chem. Phys.*, 17, 4817-4835,
521 <https://doi.org/10.5194/acp-17-4817-2017>, 2017.

522 Sullivan, S. C., Morales Betancourt, R., Barahona, D., and Nenes, A.: Understanding cirrus ice
523 crystal number variability for different heterogeneous ice nucleation spectra, *Atmos. Chem.*
524 *Phys.*, 16, 2611–2629, <https://doi.org/10.5194/acp-16-2611-2016>, 2016.

525 Umo, N. S., Murray, B. J., Baeza-Romero, M. T., Jones, J. M., Lea-Langton, A. R., Malkin, T.
526 L., O'Sullivan, D., Neve, L., Plane, J. M. C., and Williams, A.: Ice nucleation by combustion
527 ash particles at conditions relevant to mixed-phase clouds, *Atmospheric Chemistry and*
528 *Physics*, 15, 5195–5210, <https://doi.org/10.5194/acp-15-5195-2015>,

529 Venable, D. D., Whiteman, D. N., Calhoun, M. N., Dirisu, A.O., Connell, R. M., Landulfo, E.:
530 Lamp mapping technique for independent determination of the water vapor mixing ratio
531 calibration factor for a Raman lidar system, *Appl. Opt.*, 50, 4622 - 4632, 2011.

532 Veselovskii I., Kolgotin, A., Griaznov, V., Müller, D., Wandinger, U., Whiteman, D.:
533 Inversion with regularization for the retrieval of tropospheric aerosol parameters from multi-
534 wavelength lidar sounding, *Appl.Opt.* 41, 3685-3699, 2002.

535 Veselovskii, I., Whiteman, D. N., Korenskiy, M., Suvorina, A., Kolgotin, A., Lyapustin, A.,
536 Wang, Y., Chin, M., Bian, H., Kucsera, T. L., Pérez-Ramírez, D., and Holben, B.:
537 Characterization of forest fire smoke event near Washington, DC in summer 2013 with
538 multiwavelength lidar, *Atmos. Chem. Phys.*, 15, 1647-1660, <https://doi.org/10.5194/acp-15-1647-2015>, 2015.

540 Veselovskii, I., Hu, Q., Goloub, P., Podvin, T., Korenskiy, M., Pujol, O., Dubovik, O., Lopatin,
541 A.: Combined use of Mie-Raman and fluorescence lidar observations for improving aerosol
542 characterization: feasibility experiment, *Atm. Meas. Tech.*, 13, 6691–6701, 2020.
543 doi.org/10.5194/amt-13-6691-2020.

544 Veselovskii, I., Hu, Q., Goloub, P., Podvin, T., Choël, M., Visez, N., and Korenskiy, M.: Mie–
545 Raman–fluorescence lidar observations of aerosols during pollen season in the north of
546 France, *Atm. Meas. Tech.*, 14, 4773–4786, 2021. doi.org/10.5194/amt-14-4773-2021

547

548 Table 1. Conversion factors C_N , C_S , and C_V , and fluorescence capacity G_F at height H for five
 549 smoke episodes. Volume and surface area concentration of smoke particles, obtained by the
 550 inversion of $3\beta+2\alpha$ lidar observations (V , S), are given together with values calculated from
 551 fluorescence measurements (V^S , S^S) and using conversion factors (Eq. 4).

Date dd/mm/yy	H , km	C_{N_s} $10^4 \frac{cm^{-3}}{Mm^{-1}sr^{-1}}$	C_{S_s} $10^4 \frac{\mu m^2 cm^{-3}}{Mm^{-1}sr^{-1}}$	C_{V_s} $10^4 \frac{\mu m^3 cm^{-3}}{Mm^{-1}sr^{-1}}$	G_{F_s} 10^{-4}	$V, \mu m^3/cm^3$		$S, \mu m^2/cm^3$	
						V	V^S	S	S^S
23/06/20	4.9	88	35	2.4	3.5	21 ± 4	19 ± 4	306 ± 75	237 ± 60
11/09/20	7.5	75	28	2.0	3.9	7.6 ± 1.6	8.7 ± 1.6	111 ± 25	111 ± 25
14/09/20	6.0	90	34	2.3	3.7	6.4 ± 1.3	6.1 ± 1.3	94 ± 25	78 ± 20
17/09/20	6.8	21	21	2.3	2.9	8.0 ± 1.6	7.8 ± 1.6	73 ± 18	100 ± 25
20/09/20	4.9	33	22	2.0	4.3	2.7 ± 0.5	2.9 ± 0.6	31 ± 8	37 ± 9

552

553

554

555

556

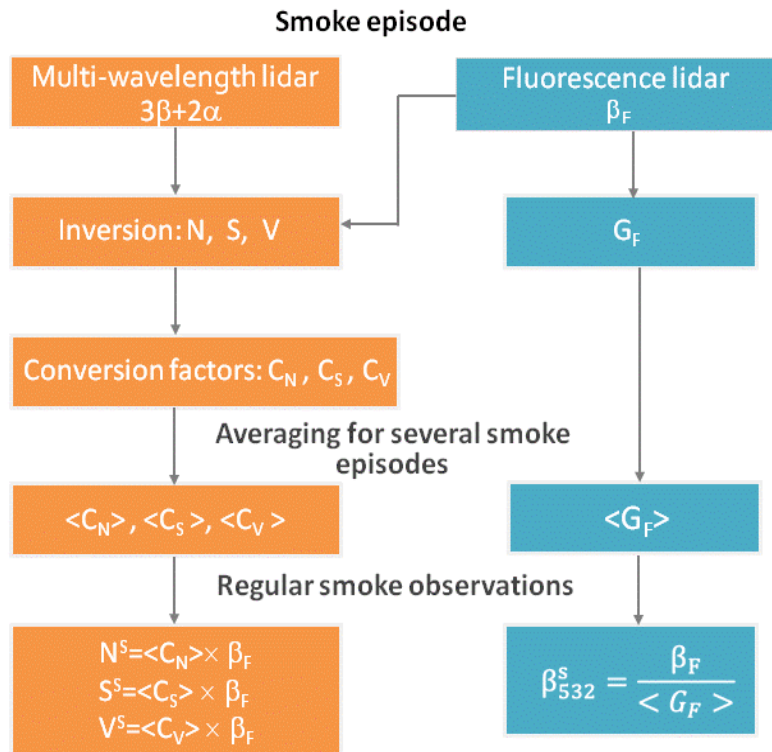
557 Table 2. Number N^S , surface area S^S , and volume V^S concentrations of smoke particles inside the
 558 ice cloud at height H estimated from fluorescence measurements by applying the conversion
 559 factors in Eq. (4) for four measurement sessions.

Date dd/mm/yy	Time UTC	H , km	β_F , $10^{-4} Mm^{-1}sr^{-1}$	N^S , cm^{-3}	S^S , $\mu m^2/cm^3$	V^S , $\mu m^3/cm^3$
12/09/20	01:20-01:45	10.5	0.32	20 ± 10	9 ± 2.3	0.7 ± 0.15
12-13/09/20	21:00-03:00	12.5	0.06	3.5 ± 1.8	1.6 ± 0.4	0.13 ± 0.03
17/09/20	22:45-23:45	8.5	6.5	400 ± 200	180 ± 45	14 ± 3
24-25/11/20	18:00-06:00	8.0	0.013	0.8 ± 0.4	0.36 ± 0.09	0.03 ± 0.006

560

561

562 **Appendix A.** Estimation of smoke parameters from Mie-Raman and fluorescence lidar
 563 measurements.

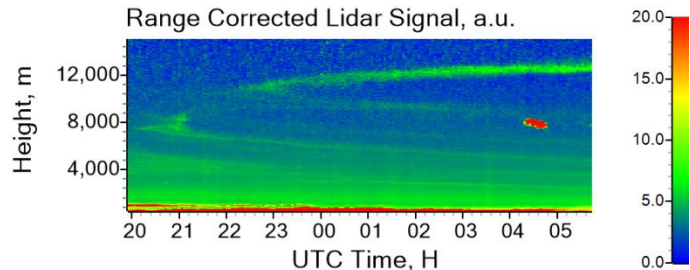


564
 565 Fig.A. Flow chart showing the main steps of the procedure of smoke parameters estimation from
 566 multiwavelength Mie-Raman and fluorescence lidar measurements. Procedure includes the
 567 following steps. (i) For a strong smoke layer the $3\beta+2\alpha$ data set, derived from multiwavelength
 568 Mie-Raman lidar observations, is inverted to the particle number N , surface S and volume V
 569 density. (ii) Conversion factors C_N , C_S , C_V are calculated from Eq.(3) by using the fluorescence
 570 backscattering coefficient β_F . (iii) Different smoke events are analyzed to get mean values of
 571 conversion factors $\langle C_N \rangle$, $\langle C_S \rangle$, $\langle C_V \rangle$. These mean values are used to estimate smoke
 572 concentration in weak layers in UTLS and inside cirrus clouds in regular observations. The mean
 573 value of smoke fluorescence capacity $\langle G_F \rangle$ allows estimation of smoke contribution β_{532}^s to the
 574 total backscattering coefficient β_{532} .

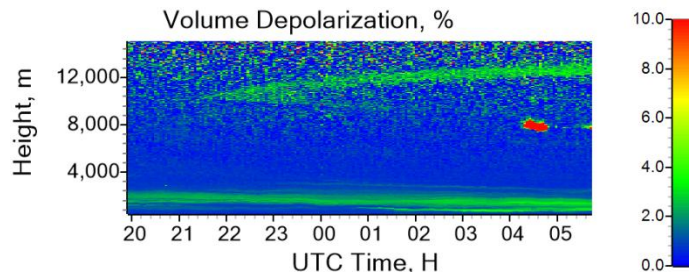
575

576

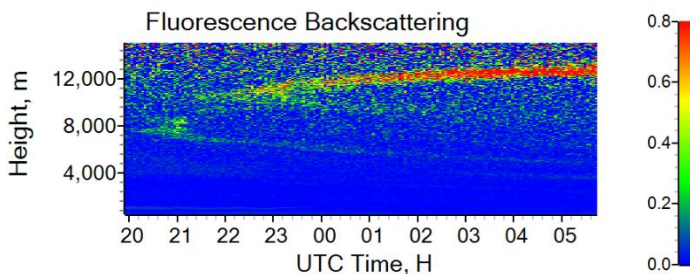
577



578



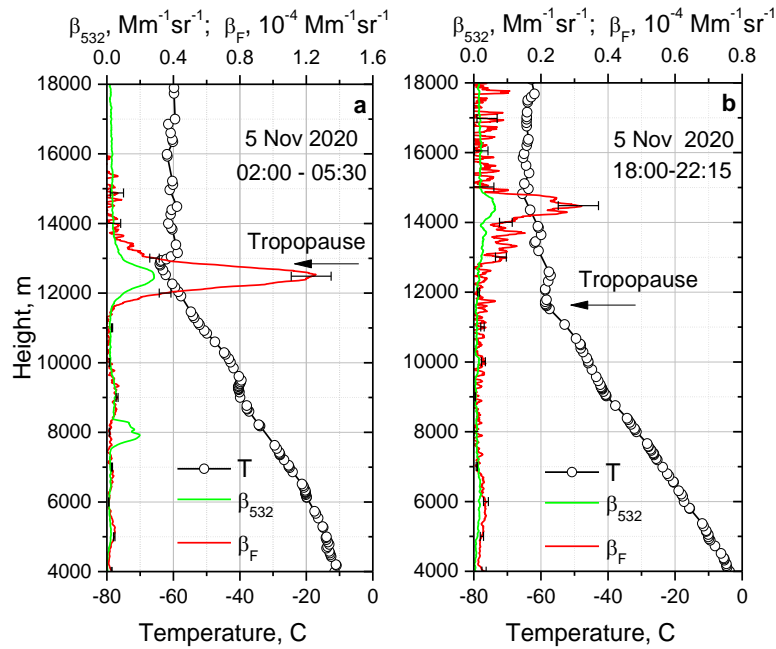
579



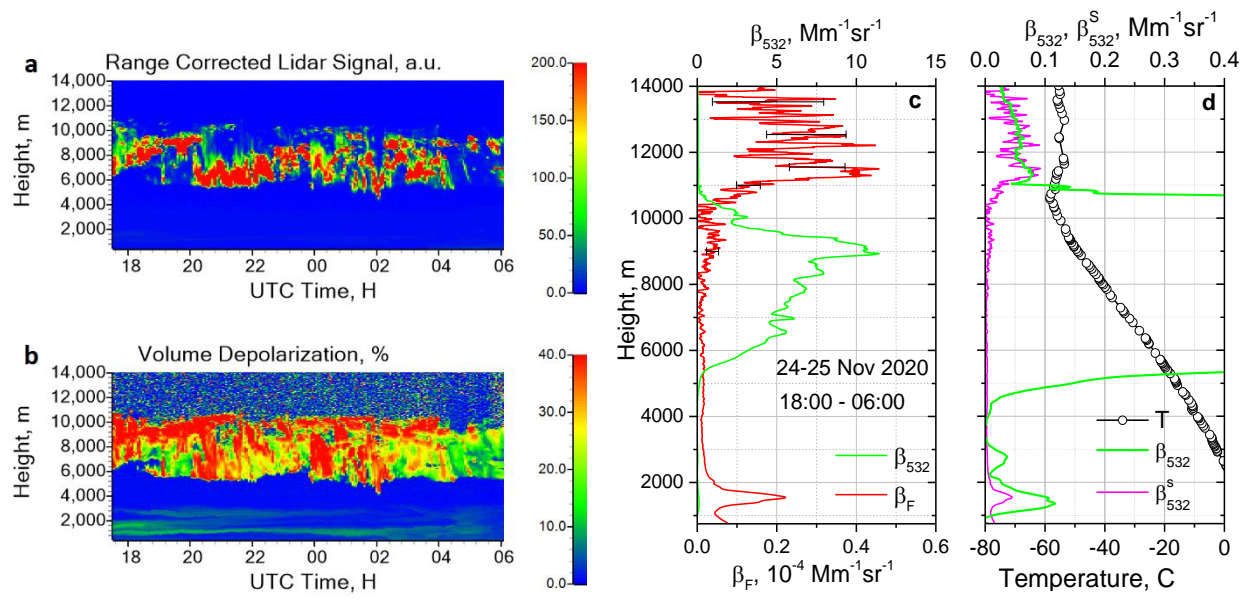
580

581 Fig.1. Range corrected lidar signal at 1064 nm, volume depolarization ratio at 1064 nm and
582 fluorescence backscattering coefficient (in $10^{-4} \text{ Mm}^{-1} \text{sr}^{-1}$) on 4-5 November 2020.

583



586 Fig.2. Vertical profiles of aerosol backscattering β_{532} and fluorescence backscattering β_F
 587 coefficients on 5 November 2020 for the periods (a) 02:00 - 5:30 UTC and (b) 18:00 – 22:15
 588 UTC. Open symbols show the temperature profile measured by the radiosonde launched at
 589 Herstmonceux (UK).



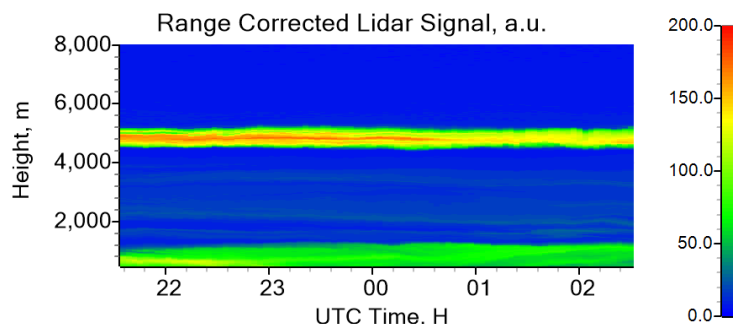
593 Fig.3. Smoke fluorescence in the presence of clouds on 24 – 25 November 2020. (a, b)
594 Spatiotemporal variations of the range corrected lidar signal and volume depolarization at 1064
595 nm. (c) Vertical profiles of the aerosol β_{532} and fluorescence β_F backscattering coefficients. (d)
596 Aerosol backscattering β_{532} together with smoke backscattering β_{532}^s coefficient, computed from
597 β_F for $G_F=4.5\times 10^{-4}$. Open symbols show temperature profile measured by the radiosonde at
598 Herstmonceux.

599

600

601

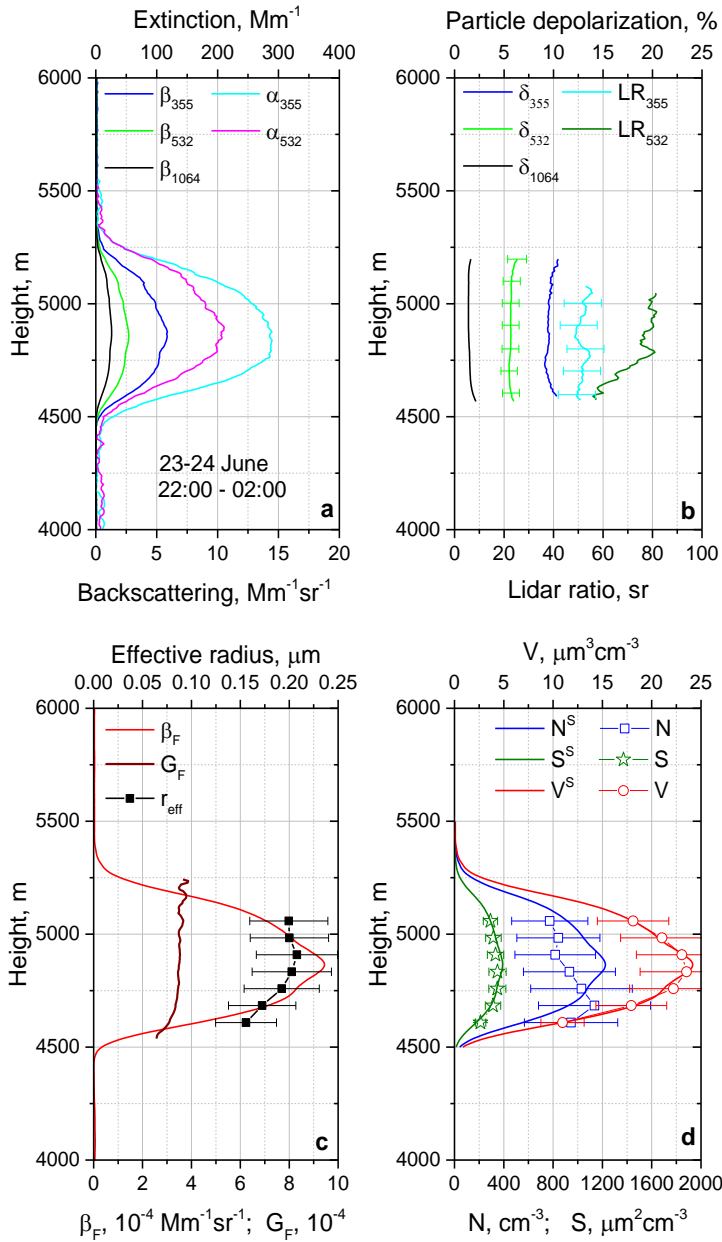
602



603

604 Fig.4. Range corrected lidar signal at 1064 nm on 23-24 June 2020, revealing a smoke layer
605 between 4500 and 5200 m height.

606



607

608

609

610

611

612

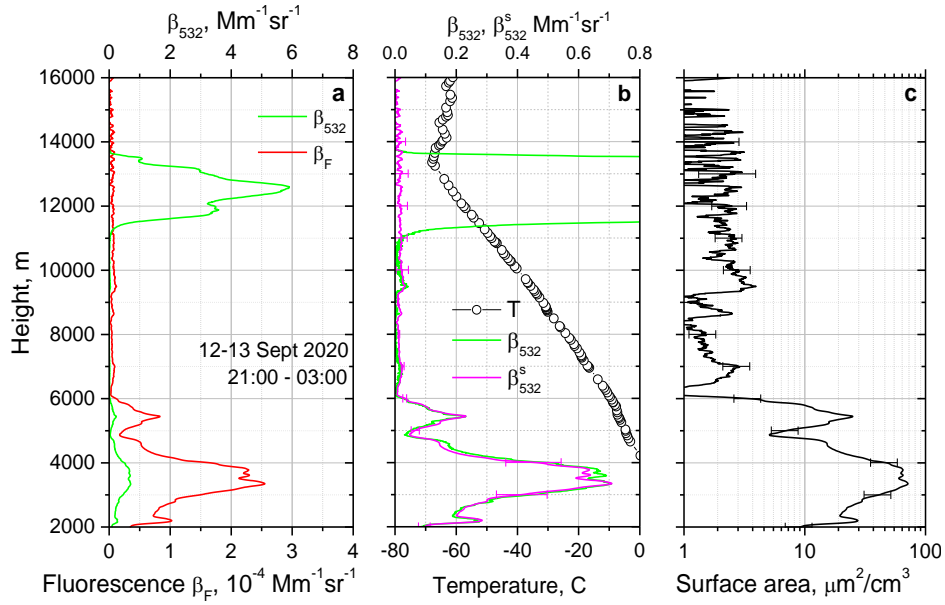
613

614

615

616

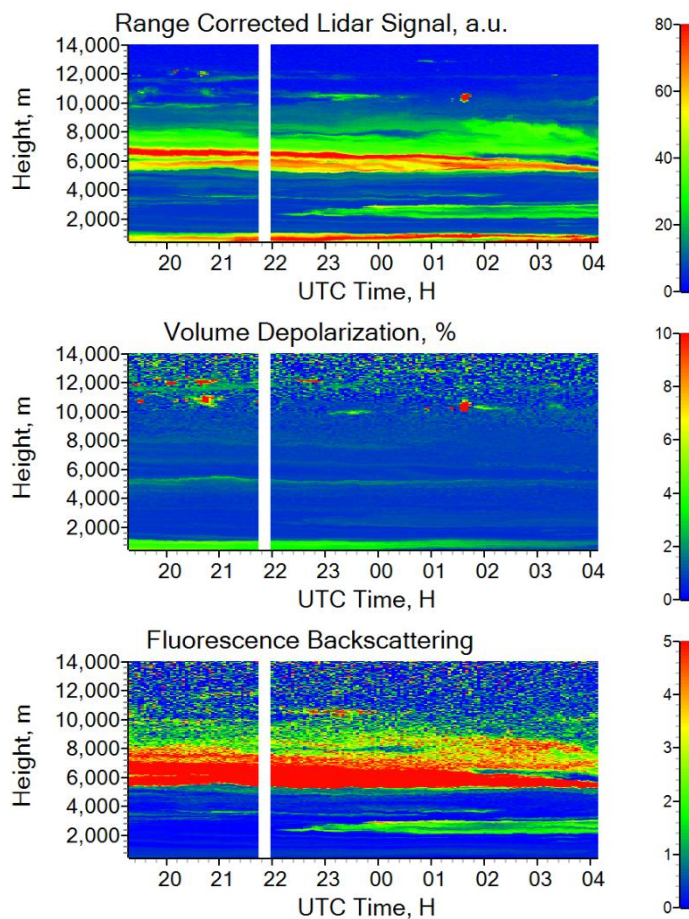
Fig.5. Smoke layer on 23-24 June 2020. (a) Vertical profiles of backscattering (β_{355} , β_{532} , β_{1064}) and extinction (α_{355} , α_{532}) coefficients. (b) Particle depolarization ratios (δ_{355} , δ_{532} , δ_{1064}) and lidar ratios (LR_{355} , LR_{532}). (c) Fluorescence backscattering (β_F), fluorescence capacity (G_F) and the particle effective radius (r_{eff}). (d) Number (N , N^S), surface area (S , S^S) and volume (V , V^S) concentrations obtained by inversion of $3\beta+2\alpha$ observations (symbols) and calculated from the fluorescence backscattering (lines) by using the mean conversion factors defined in Eq. (3).



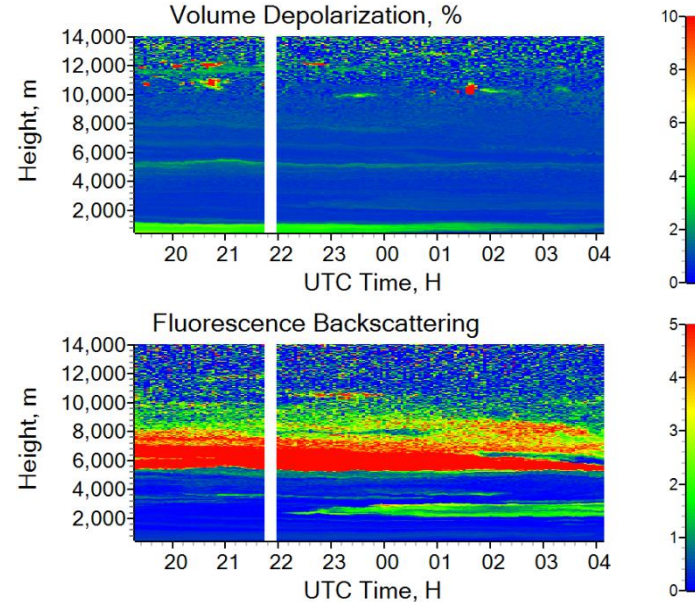
617
618 Fig.6. Observation of smoke fluorescence on 12-13 September 2020, 21:00 – 03:00 UTC. (a)
619 Vertical profiles of the aerosol backscattering β_{532} and fluorescence backscattering β_F
620 coefficients. (b) Aerosol backscattering β_{532} together with smoke backscattering β_{532}^s coefficient
621 computed from β_F for $G_F=3.6\times 10^{-4}$. (c) Surface area concentration of the smoke particles
622 calculated from β_F by using the respective conversion factor from (4). Open symbols show the
623 temperature profile measured by the radiosonde at Herstmonceux.

624
625
626

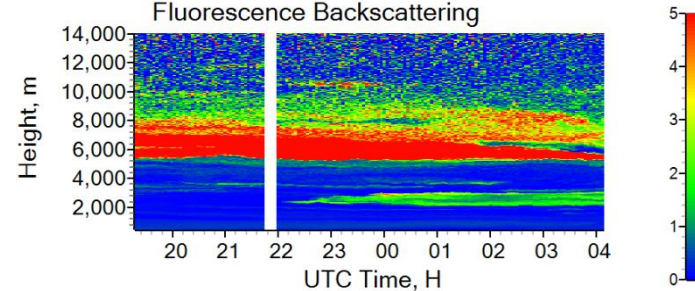
627



628



629



630

Fig.7. Formation of ice particles at heights above 10 km inside a smoke layer on 11-12 September 2020.

631

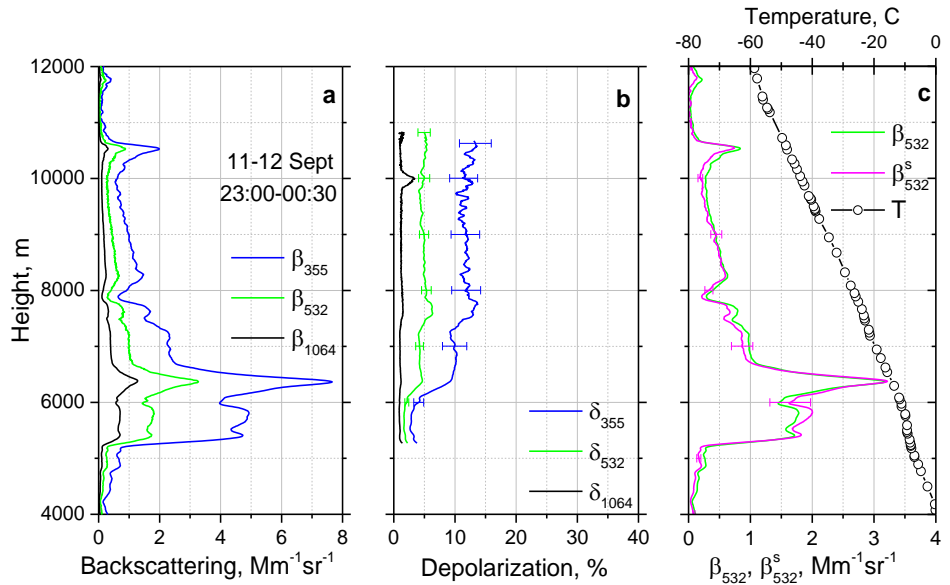
632 Spatiotemporal variations of range corrected lidar signal at 1064 nm, volume depolarization ratio at

633

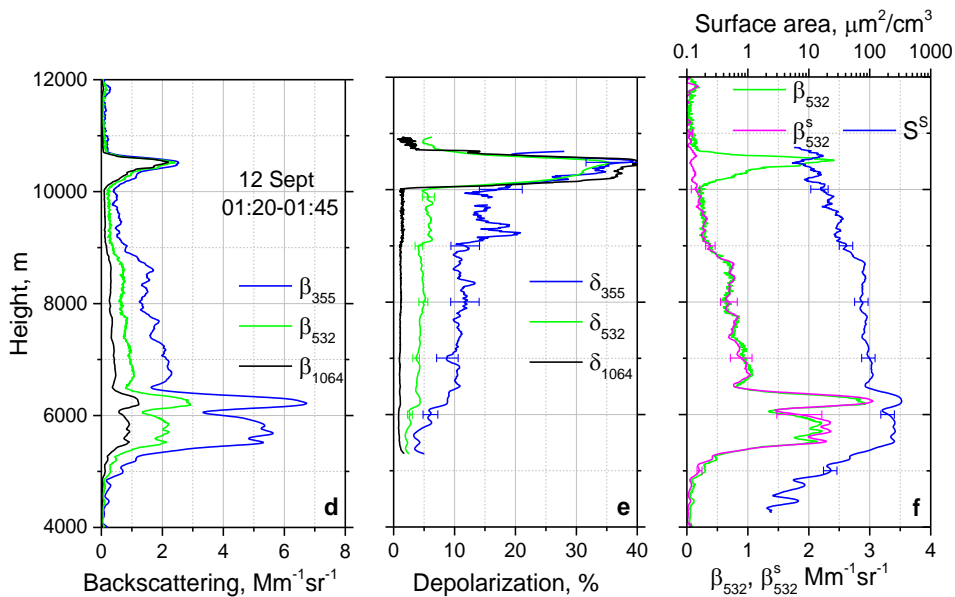
1064 nm and fluorescence backscattering coefficient (in $10^{-4} \text{ Mm}^{-1} \text{sr}^{-1}$).

634

635



636



637

638 Fig.8. Formation of ice particles at 10-11 km height inside a smoke layer on 11-12 September
 639 2020. Vertical profiles of (a, d) the aerosol backscattering coefficients β_{355} , β_{532} , β_{1064} ;
 640 (b, e) the particle depolarization ratios δ_{355} , δ_{532} , δ_{1064} ; (c, f) β_{532} together with backscattering coefficient of
 641 smoke β_{532}^s , calculated from fluorescence backscattering β_F assuming $G_F=4.0\times10^{-4}$. Plot (f)
 642 shows also the smoke surface area concentration S^s of the smoke particles calculated from β_F by
 643 applying the respective conversion factor in Eq. (4). Results are given for the time intervals
 644 23:00 – 00:30 UTC and 01:20 – 01:45 UTC: prior and during ice cloud formation at 10.5 km
 645 height. The temperature profile measured by the radiosonde at Herstmonceux is shown with open
 646 symbols in panel (c).

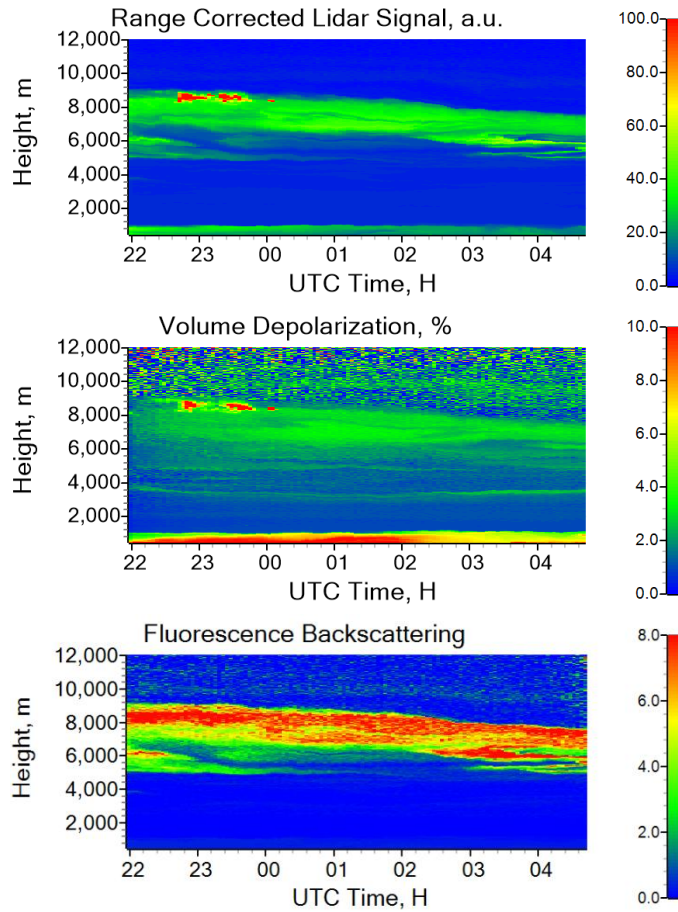
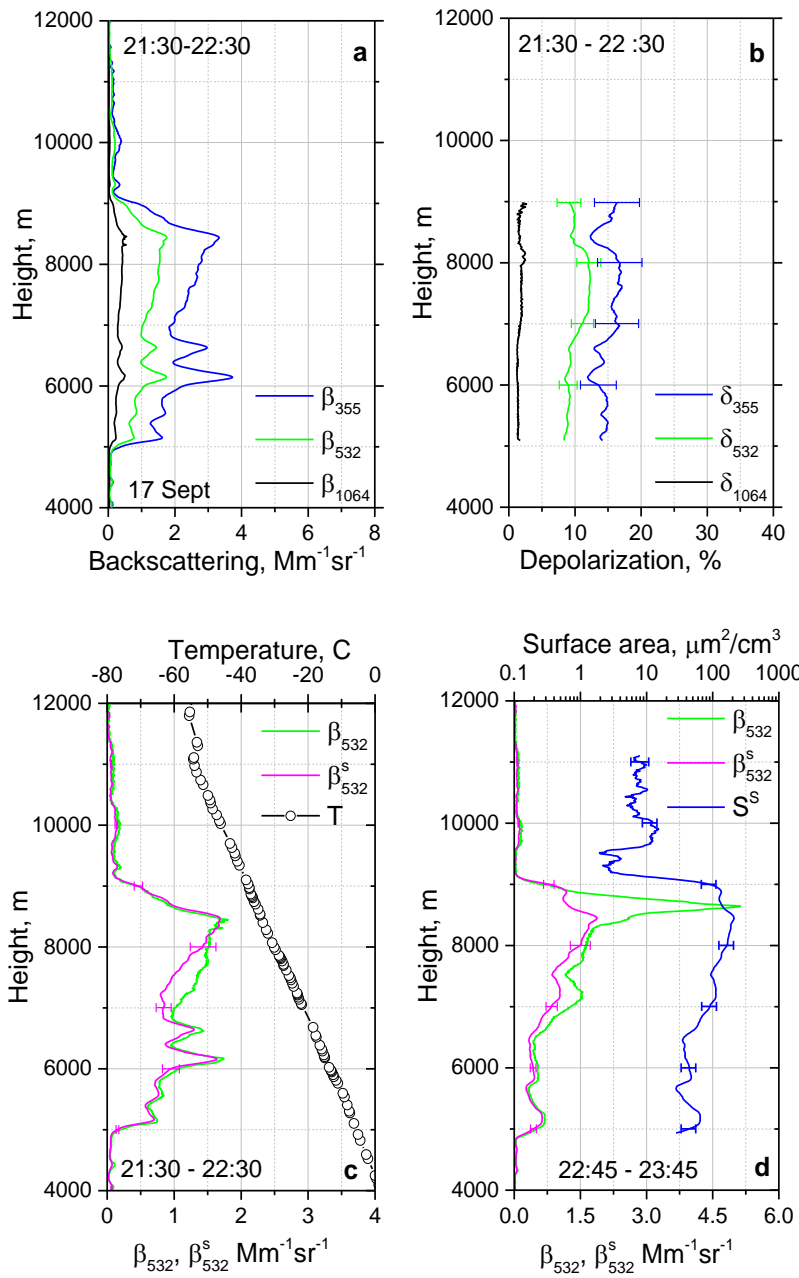


Fig.9. Formation of ice particles at heights above 8 km inside the smoke layer on 17-18 September 2020. Spatiotemporal variations of range corrected lidar signal at 1064 nm, volume depolarization ratio at 1064 nm and fluorescence backscattering coefficient (in $10^{-4} \text{ Mm}^{-1} \text{sr}^{-1}$).



656
657 Fig.10. Formation of ice particles at 8.5-8.6 km height inside a smoke layer on 17 September
658 2020. Vertical profiles of (a) the aerosol backscattering coefficients β_{355} , β_{532} , β_{1064} ; (b) the
659 particle depolarization ratios δ_{355} , δ_{532} , δ_{1064} ; (c, d) β_{532} together with backscattering coefficient
660 of smoke β_{532}^s , calculated from fluorescence backscattering β_F assuming $G_F=3.5\times 10^{-4}$. Results are
661 given for the time intervals (a-c) 21:30 – 22:30 UTC and (d) 22:45 – 23:45 UTC: prior and
662 during ice formation at 8.5 km height. Plot (d) shows also the surface area concentration of the
663 smoke particles S^s calculated from β_F by applying the respective conversion factor from (4). The
664 temperature profile measured by the radiosonde at Herstmonceux is shown with open symbols in
665 panel (c).
666